Fiber-Based Multi-Resolution Imaging and Multidimensional X-ray Diagnostics for Ejecta Dynamics in Plume Surface Interactions

Lucca M. de Carvalho *, Kanan Karimli†, Rees P. Verleur ‡, Amanda M. Braun §, Venkat Athmanathan ¶, Mikhail N. Slipchenko ‖, Terrence R. Meyer**
School of Mechanical Engineering, Purdue University, West Lafayette, IN 47907, USA

Naibo Jiang ††, Paul Hsu ‡‡, Sukesh Roy §§
Spectral Energies, LLC, 4065 Executive Dr, Beavercreek, OH 45430, USA

Neil S. Rodrigues ¶¶, Paul M. Danehy ***
NASA Langley Research Center Hampton, VA, 23666, USA

The interaction of a rocket exhaust plume with a particulate-laden surface creates a complex, multiphase flow field that can destabilize the vehicle and damage nearby equipment. This study investigates two methods for capturing the particulate dynamics of plume-surface interaction (PSI): optical fiber-based multi-resolution Mie scattering and multi-dimensional X-ray radiography. Mie scattering was used to track PSI-interacted particles, trace their paths, and measure velocities. While effective for the jet periphery and early PSI stages, the technique becomes limited as the scattering cross-section increases over time due to particle displacement from the soil bed, causing the core to become optically dense and appear as a luminous, opaque region. To address this, X-ray radiography was explored as a complementary method for visualizing the optically dense core. PSI experiments were conducted with both reacting and non-reacting jets to evaluate these approaches across a range of optical and flow parameters. The results demonstrated the capability of the fiber-based multi-resolution imaging system to capture simultaneous fields of view at varying magnifications (1x, 2x, 4x), and the ability of X-ray imaging to penetrate the optically dense plume, revealing flow structures that would otherwise be obscured in scattering-based methods. Data were collected for various PSI parameters, including three different heights above the surface, to analyze the ejecta properties and the plume's temporal evolution. These results provide the first imaging strategy capable of resolving flow structures over a wide spatial dynamic range while also offering the first visualization of the optically dense core.

I. Nomenclature

ϕ = equivalence ratio
D = nozzle exit diameter
h = height above particle bed
$\dot{m}$ = mass flow rate

*Graduate Student, School of Mechanical Engineering
†Doctoral Student, School of Aeronautics and Astronautics
‡Doctoral Student, School of Aeronautics and Astronautics
§Postdoctoral Research Associate, School of Mechanical Engineering, AIAA Member. (Currently, Postdoctoral Fellow in the NASA Postdoctoral Program)
¶Senior Research Scientist, School of Mechanical Engineering
‖Research Full Professor, School of Mechanical Engineering
**Professor, School of Mechanical Engineering and School of Aerospace and Aeronautics (by Courtesy)
††§Senior Research Scientist Spectral Energies, LLC., AIAA Associate Fellow
‡‡§Senior Research Scientist Spectral Energies, LLC., AIAA Associate Fellow
§§§Senior Research Scientist and CEO, Spectral Energies, LLC., AIAA Associate Fellow
¶¶Optical Physicist, Advanced Measurements and Data Systems Branch, AIAA Member
***Senior Technologist, Advanced Measurements and Data Systems Branch, AIAA Associate Fellow

II. Introduction

The phenomenon of plume-surface interaction (PSI) has garnered significant attention, especially with the renewed focus on lunar exploration through NASA's Artemis missions. When a high-velocity jet approaches a particulate-laden surface, such as a lunar lander descending to the moon, two interconnected phenomena occur: crater formation and the ejection of high-speed particles, together resulting in a complex multiphase flow [1]. These interactions can exert forces on the lander, generate unexpected heat flux, and damage sensitive components, including optical windows, thermal protection systems, and tracking sensors [2–4]. Cratering caused by PSI poses additional risks to successful lander touchdown. Craters formed by PSI can drastically alter the terrain of the landing zone, which can lead the lander to exceed its tilt limits upon touchdown, endangering astronauts and scientific equipment, and contaminating surface samples in designated research areas [5, 6]. The increasing mass of modern commercial landing systems necessitates larger retro-propulsive boosters, making PSI an even more critical concern for upcoming missions [7].

Shock wave formation in the rocket exhaust plume is a key feature of PSI. In the near-vacuum environment of the moon or low-pressure planetary atmospheres like Mars, the exhaust expands beyond the nozzle exit, creating a shock train before impinging on the regolith surface [8]. Initially, the interaction resembles a steady impinging jet on a flat plate, where critical flow structures such as plate shocks and tail shocks form [9]. Beneath the plate shock, high-pressure recirculation zones, stagnation bubbles, and high-velocity ejecta develop [9]. These flow structures interact with soil erosion mechanisms, such as viscous erosion, and bearing capacity failure, resulting in a highly interconnected problem involving plume flow, granular flow, and rarefied flow [10, 11].

Research into the flow physics of PSI have relied on numerical, analytical, and experimental studies. In the 1960s, Roberts [12, 13] conducted pioneering analytical studies on plume impingement for the Apollo missions, constrained by limited computational resources. Advances in computational power have since enabled detailed numerical modeling. For example, Morris et al. [14] used a hybrid solver to simulate PSI for a single and four-nozzle lunar lander, while Chinnappan et al. [15] developed a two-way coupled gas-grain interaction model using the direct simulation Monte Carlo (DSMC) method. Recent efforts by Cao et al. [16] introduced new methods to model multiphase flows involving rarefied gases.

Experimental studies followed soon after Roberts' numerical work. Landmark experiments by Land and Clark in 1965 investigated erosion dynamics and crater formation under vacuum conditions but failed to adequately characterize ejecta due to dense clouds obstructing observation [17]. Subsequent studies by Metzger et al. [18] examined cratering dynamics under subsonic and supersonic plumes. Recent experimental studies at NASA in low-pressure vacuum environments have been documented by Refs. [2, 8, 10, 19–24]. Among these were the highly relevant studies by Diaz-Lopez et al. [19] and Rubio et al. [2] where scaled, low-pressure experiments were performed and high-speed imaging was used to analyze cratering and ejecta phenomena.

Imaging techniques such as computed tomography (CT) have been extensively applied to study exhaust plumes and sprays, although they have limited ability to resolve complex particle-scale flow interactions. Furthermore, line-of-sight path-averaged techniques often encounter limitations in optically dense or absorptive media [25–27]. In such cases, X-rays offer significant advantages due to their ability to penetrate through dense media, enabling visualization of ejecta and transient structures in exhaust jets [27]. X-ray CT, introduced in 1972 for clinical applications [28], has been adapted for various research domains, including fuel spray and plume analysis. Key milestones include the first 2D X-ray CT analysis of a fuel spray in 2003 [29], 3D reconstructions of hollow-cone sprays in 2009 [30], and validation of numerical models for two-phase flows [31]. Recent advancements, such as the multi-hole gasoline injection spray imaging by Duke et al. [32] and the imaging of reactive solid propellants by Collard et al. [33], highlight the robustness and versatility of X-ray diagnostics for complex flow environments.

This study seeks to address the current gap in experimental PSI research through two approaches. The first is simultaneous multi-resolution planar Mie imaging using fiber scopes to track the flow at the particle scale. The second is to utilize X-ray diagnostics to penetrate the dense ejecta cloud and visualize internal flow structures. By combining advanced imaging methods with X-ray imaging, this work aims to provide novel insights into plume dynamics and enhance the experimental dataset available for PSI studies. These methods are evaluated for plume impingement on a particle bed using both a custom-made supersonic burner for the Mie imaging and a a cold gas jet for the X-ray imaging.

III. Experimental Setup

A. Multi-Resolution Visible Light Scattering Experiment

1. Imaging System

To capture the complex multi-phase phenomena, a set of three ultra-high-resolution fiber bundles with one million fibers per bundle were used to combine images from various fields of view into a single view for 2D velocimetry measurements at rates of up to 100 kHz. This method allows one camera chip to capture up to four different fields of view, allowing for simultaneous, synchronized imaging of a range of scales from particulates to large ejecta structures. The fiberscope ends were connected to camera lenses using threaded mounts. Two ends used a 200 mm lens and the third end used a 105 mm lens. The camera used for this approach was a Phantom® TMX-7510 coupled with a 200 mm lens at f/4. For this test campaign, the camera frame rate was set to 76 kHz at a full-frame resolution of 1280x800 pixels and an exposure time of 1 µs. Each fiber bundle collected a different field of view within the flow using various camera lenses, and each image was transmitted to the other end of the fiber to be imaged by the TMX camera. Each fiber was viewing at an angle of < 15° from the imaging plane to minimize distortion. The fiberscope imaging layout is illustrated in Figs. 1 and 2.

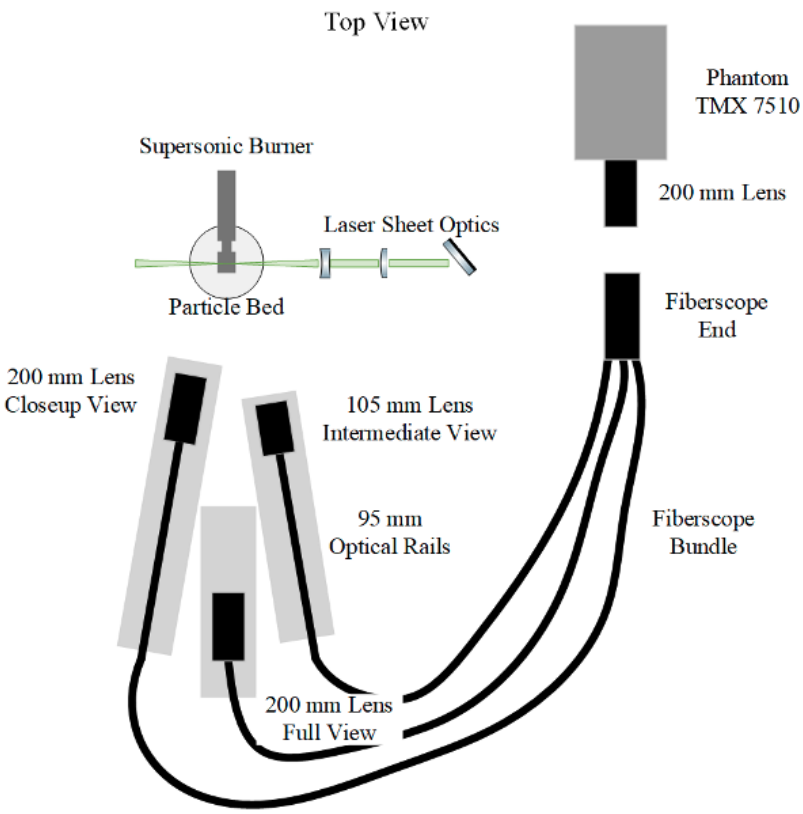

Fig. 1 Fiberscope imaging layout from the (left) top view and (right) side view.

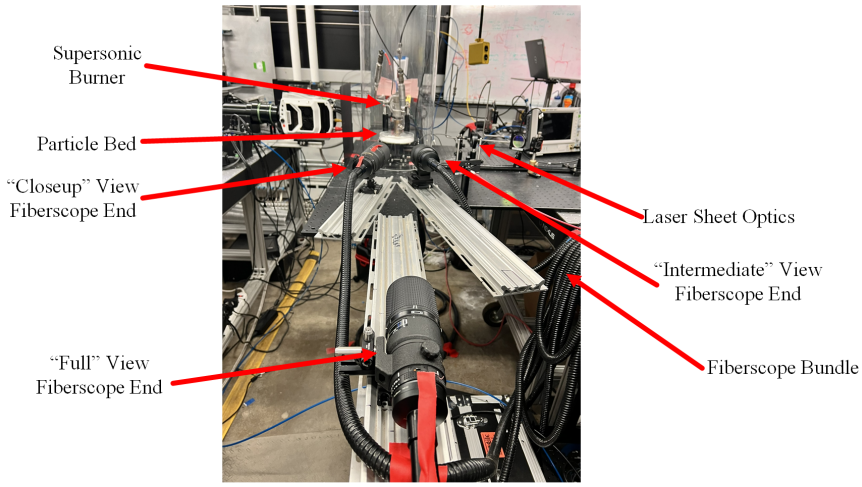

Fig. 2 Photograph of PSI test setup with fiberscopes.

The three views will be called "Closeup," "Intermediate," and "Full" to refer to the varying domain sizes captured in each view. Table 1 below quantifies the lenses and f-stops used for the three different fiberscope views and their spatial resolutions as measured by a USAF 1951 test chart.

Table 1 Fiberscope imaging and resolution parameters.

	Lens [mm]	f-stop	Resolution [mm/px]	Zoom
Full View	200	f/4	0.140	1x
Intermediate View	105	f/5.6	0.063	2.1x
Closeup View	200	f/8	0.035	4.4x

Here, the zoom is computed relative to the full view. The f-stops were set to maximize signal levels while maintaining focus for the whole field of view.

2. Laser Illumination System

To accurately measure the velocity of the ejecta from the PSI, the particle-image velocimetry (PIV) technique was employed with planar laser-sheet illumination using the output of a frequency-doubled burst-mode laser. The burst-mode laser was operated at 76 kHz with a 10.5 ms burst duration, yielding ~750 pulses, and the energy was kept at ~1 mJ/pulse at 532 nm. A mirror was used to direct the laser beam parallel to the imaging plane. An f = 300 mm plano-convex lens and an f = -50 mm cylindrical lens were used to create a laser sheet. The laser sheet was ~500 µm thick with a height of 62 mm. The sheet height allowed for illumination of the entire field of view across the ranges of jet heights with respect to the particle bed. Figure 3 below illustrates the orientation of the laser sheet optics.

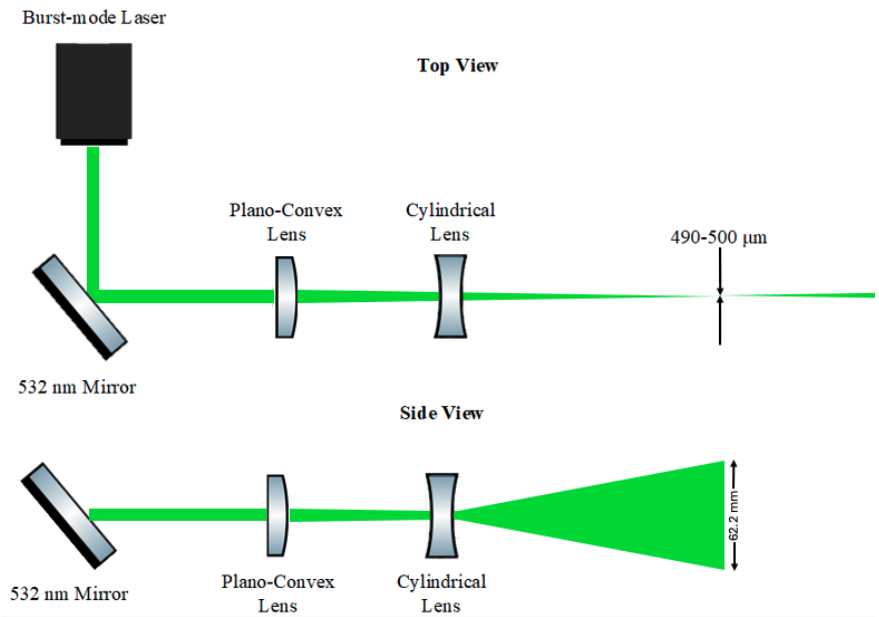

Fig. 3 Laser sheet optics for PIV measurements.

3. Hot-gas Supersonic Flow System

To emulate the PSI flow field, an under-expanded supersonic CH_4/air jet plume was created by a two-stage vitiated combustor derived from Karpetis et al. [34]. In the first stage, a lean CH_4/air flame generated hot, vitiated combustion products. This stage features essential components such as a combustion liner, a V-gutter for flame stabilization, and a spark igniter for ignition. The hot and vitiated combustion products from the first stage are used in the second stage. By adding CH_4 in the second stage, the remaining hot oxygen left over from the fuel-lean first stage is consumed. The mixture generated in the second stage is then passed through a converging nozzle with a throat diameter of 3.5 mm. Figure 4 details the components of the supersonic burner along with an image taken with a digital camera illustrating the supersonic jet.

Additional components were added to ensure safe and remote operation of the supersonic burner. One such addition was the instrumentation for condition monitoring during the burner operation. This includes first and second-stage pressure transducers and temperature measurements at the exhaust of the second stage. Remotely operated mass flow controllers (MFCs) were also integrated into an automated data acquisition system (DAQ) to control flow into both the first and second-stage fuel inlets and the first-stage air inlet. The DAQ also allowed for remote monitoring of pressure transducer and thermocouple data along with the capability to set up an automated firing sequence that was synchronized with both the imaging and laser illumination systems.

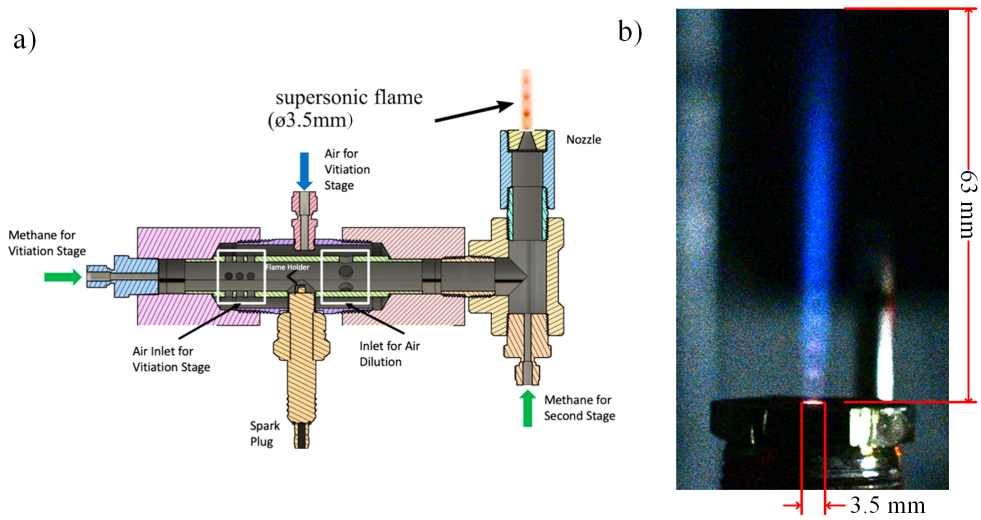

Fig. 4 a) Cross-sectional annotated view of the supersonic burner. b) Broadband chemiluminescence of the supersonic jet.

Table 2 shows the burner mass flow rates and equivalence ratios (ϕ) used for all of the PSI tests. These parameters were chosen after determination of conditions that created the most stable supersonic jet.

Table 2 Final Burner Flow Parameters.

Air $\dot{m}$ [g/s]	Stage 1 CH_4 $\dot{m}$ [g/s]	Stage 2 CH_4 $\dot{m}$ [g/s]	Stage 1 ϕ	Stage 2 ϕ
3.7	0.14	0.31	0.68	2.14

Timing the camera, laser, and burner was a crucial step in ensuring that the PIV captured the exact moment the plume hit the surface of the particle bed. To do this, the high-speed camera was used as the master clock to trigger the laser from the camera exposure signal. The camera was connected to the DAQ using a relay and was triggered by a LabView® Virtual Instrument (VI). In the VI, an auto sequence was created to trigger the camera as the combustion gases were exiting the nozzle of the burner.

4. Testing Parameters

The test parameters for this multi-resolution imaging setup covered a range of variables important for PSI testing. The first is *h/D*, which is the height of the nozzle above the particle bed divided by the nozzle exit diameter, where D is 3.5 mm for the current burner. This variable has been shown to affect ejecta trajectories and velocities in prior work [1, 8, 11] .

The other key variable that was varied in this campaign was the particle size. For these tests, solid soda lime glass microspheres with a fluorochemical coating were used. The fluorochemical coating increased the hydrophobicity of the spheres, which prevented clumping due to moisture. Two microspheres of different sizes were used. The first had a median diameter of between 8 and 12 microns ("small" particles), and the second had a median diameter of between 65 and 75 microns ("large" particles). This variation in size enabled the investigation of the influence of particulate size on ejecta velocities and trajectories. The size of the particulates is on the same scale as the size of Martian and lunar regolith while still maintaining a large enough diameter to avoid handling issues with the particulates. Having two different size ranges also allowed for the particulates to be mixed together ("mix" particles), which created a size distribution that would better resemble lunar regolith than uniform particle size [35]. Table 3 below summarizes the test matrix for these tests.

Table 3 Test Matrix.

	Particle Type	*h/D*
Test 1	Small	3
Test 2	Large	3
Test 3	Mix	3
Test 4	Small	10
Test 5	Large	10
Test 6	Mix	10
Test 7	Small	18
Test 8	Large	18
Test 9	Mix	18

B. X-ray Radiography Setup

1. X-ray Diagnostic System

The X-ray system was comprised of three radiography systems where each system includes an X-ray tube source and detection system, as shown in Fig. 5. The Varian® RAD-60 sources had rotating tungsten anodes and two selectable focal spot sizes of 0.3 mm and 0.6 mm with an emission half-cone angle of 12°. The high-flux sources generated X-rays with a spectral range from 10 keV up to the operating voltage between 40 kV and 120 kV. The rotating-anode sources allowed for kHz-rate imaging for 0.1-1.0 s. The 50x50 mm^2, 150 µm thick cesium iodide scintillators (Hamamatsu® J8978, J6677-01, and J8734) were used to convert the X-ray photons to visible light photons for collection by the cameras. Light from the scintillators was reflected up towards the cameras using a 50x50 mm^2 square reflecting prism. This configuration reduced the number of background X-rays on the detector. The configuration also allowed for multiple viewing angles around the object of interest and a small footprint for the lead enclosure used to protect users from exposure to radiation. Images were captured at a resolution of 1920x1200 pixels with a repetition rate of 1 kHz and exposures on the order of 1 ms with three separate cameras (Phantom® VEO640s, MIRO R321S, and MIRO M320s). The spatial resolution is often determined by measuring the 10% to 90% width of the edge spread function obtained by imaging a fast-rising edge [36]. Prior work using this method found the spatial resolution of this system to be 350 µm [37].

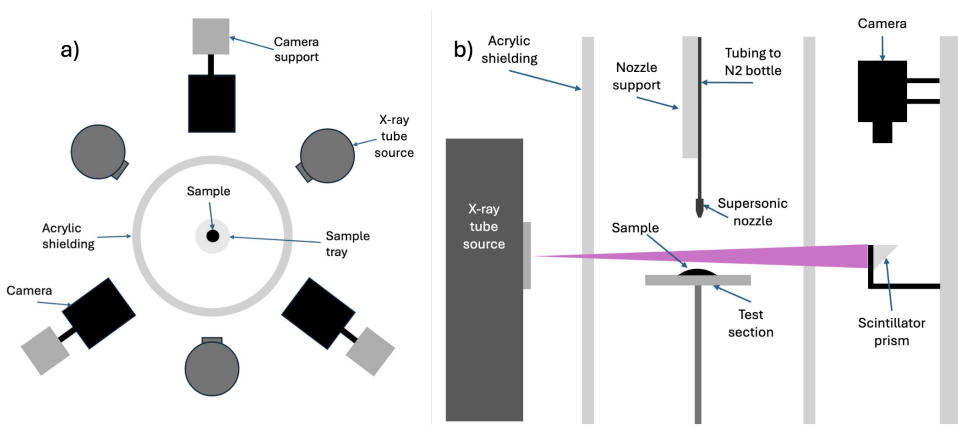

Fig. 5 a) Top view of the X-ray setup and b) cross section of imaging setup.

Figure 6 shows reference images of a screw head and thread that were used for camera focusing. Images from the X-ray sources with larger anodes (Views 1 and 2) appeared less focused. In testing, this was resolved by configuring the X-ray sources to the smaller focal spot size, leading to improved image quality. A stage holding the screw in Fig. 6 was introduced in the test area, positioned halfway between each source and its corresponding detector, to facilitate precise

alignment and later hold the test sample. Considering the conical geometry of the beam and the detector size (50 mm), this arrangement resulted in a reconstruction volume of a cylinder measuring 25 mm in diameter and 25 mm in height.

Fig. 6 Representative screw thread images from the X-ray sources. Left to right; View 1, 2 and 3.

2. Particulate Optical Density Measurements

When imaging a plume, a powder with sufficient absorption of X-rays must be used. To test the optical density (OD) of the various powders, a test jig containing path lengths between 1/16" and 1/2" was designed and 3D printed. The CAD for the jig is below in Fig. 7 along with a picture of the jig partially filled with tungsten powder.

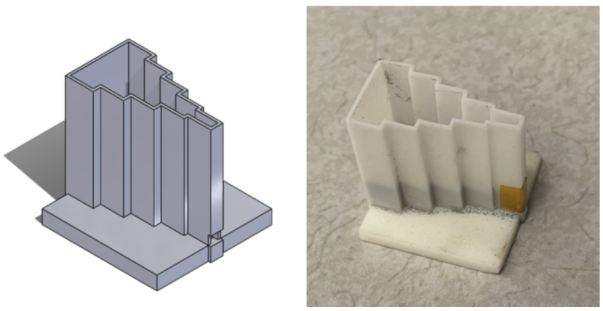

Fig. 7 X-ray path length test jig design (left) and test jig partially filled with tungsten powder (right).

The effect of the jig walls was subtracted by partially filling it so that an empty region would appear in the image along with the filled region at the bottom. Two particulates were tested for X-ray absorption: the silica glass microspheres described in III.A.4 and tungsten powder with a mean diameter of ~100 µm. The tungsten particulate size was chosen to ensure visibility in the X-ray testing environment. While lunar regolith has a variety of sizes, the data gathered from CT of the ejecta would serve to develop a scalable model for different particulate sizes. The test jig was filled with material and placed inside the test area. The glass microspheres were selected to match the corresponding scattering PSI experiment. Images were taken with the X-rays to measure OD with respect to media thickness. The resulting images are shown below in Fig. 8, labeled with the path length of each section.

From these images it was concluded that glass microspheres have too low of an absorption to appear when finely dispersed in air. The tungsten particles exhibit a notably high OD compared to the silica glass, making them much more suitable for absorption of X-rays. The use of tungsten prohibited direct comparison with the PSI scattering study conducted as part of this research. However, this work still provides cursory information on the PSI "inner core" interaction, highlighting details that may not be captured by the Mie scattering measurements.

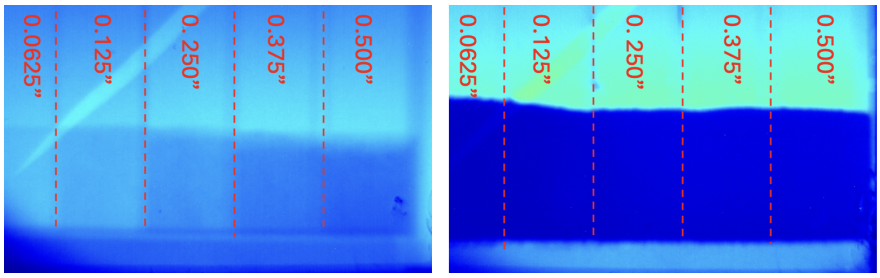

Fig. 8 X-ray radiography of glass microspheres (left) and tungsten powder (right). Measurements in red denote the width of the powder bed in that section.

3. Cold-gas supersonic flow system

The hot-gas supersonic stream was extensively utilized in the laser-scattering experiments. However, integrating this system into the X-ray imaging setup proved challenging due to space constraints at the X-ray imaging station. To address this limitation, a cold-gas thruster was used as an alternative for studying the optically dense core of the PSI, particularly during the mid-to-late stages of the interaction.

To create the necessary conditions for a PSI, a cold supersonic jet was used to simulate the supersonic exhaust of an extra-terrestrial lander. To do this, a nitrogen bottle was attached to a supersonic nozzle which operated with an exit Mach number of ≈ 3 with a plenum pressure of 250psi. The nozzle has a supersonic area ratio of 4, a throat diameter of $\approx 2.5mm$, and the contour is shown in figure 9. The effective pressure ratio is ≈ 18.7 which leads to an exit pressure of 19.7 psi, leading to a slightly underexpanded condition to minimize any additional shock diamond formation near the exhaust. A regulator was placed on the nitrogen bottle to supply nitrogen at that pressure to the nozzle. A manual ball valve was also added between the regulator and the nozzle for control of the supersonic flow during the experiment. Figure 10 below illustrates the fluid systems used for this test period.

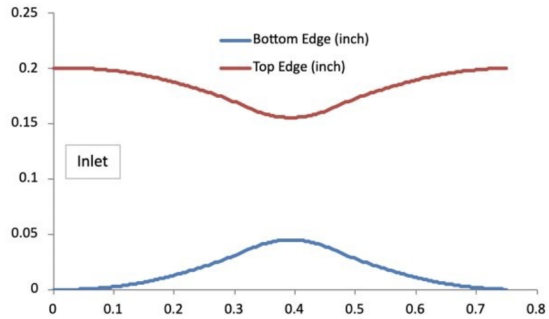

Fig. 9 Supersonic nozzle contour.

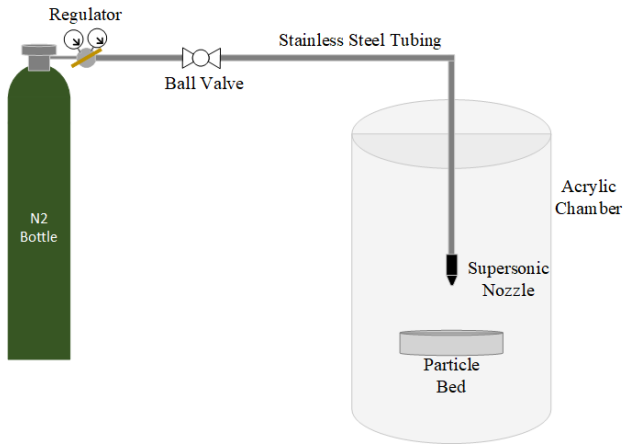

Fig. 10 Supersonic flow system schematic.

4. Testing Parameters

The only independent variable for the X-ray experiment was *h/D*, and the same values as the Mie scattering experiment were investigated. The nozzle height was manually adjusted to the *h/D* heights of 3, 10, and 18 above a circular bed of tungsten powder approximately 3 mm deep and 2.5 cm in diameter. The plenum pressure for the nozzle was kept constant at 250 psi. Valve actuation and X-ray triggering were timed and operated manually, with the X-ray source serving as a trigger for the cameras, and the jet being operational for the entirety of the X-ray exposure which was on the order of a quarter of a second. To ensure that the PSI event was adequately captured, the camera captured multiple seconds of images. The cameras were set to record at 1 kHz with an exposure of 990 µs using a 50 mm lens at f/1.8 to maximize signal.

IV. Results and Discussion

A. Mie Scattering Results

1. Raw Data Analysis

An initial qualitative analysis was conducted on the raw data from the Mie scattering experiment to demonstrate how the variable *h/D* and particle size changed the ejecta flow field properties. Figure 11 illustrates the initial impact of the three different particle sizes at approximately the same time after plume impingement at an *h/D* of 3. Although there are changes in the ejecta shape due to the structure of the particle bed surface, there are no major visible changes in the ejecta plume cloud structure due to the particle size, which may otherwise be important in interactions in low gravity and vacuum environments. Another interesting feature of the interaction is the development of the ejecta cloud over time, as shown in Fig. 12.

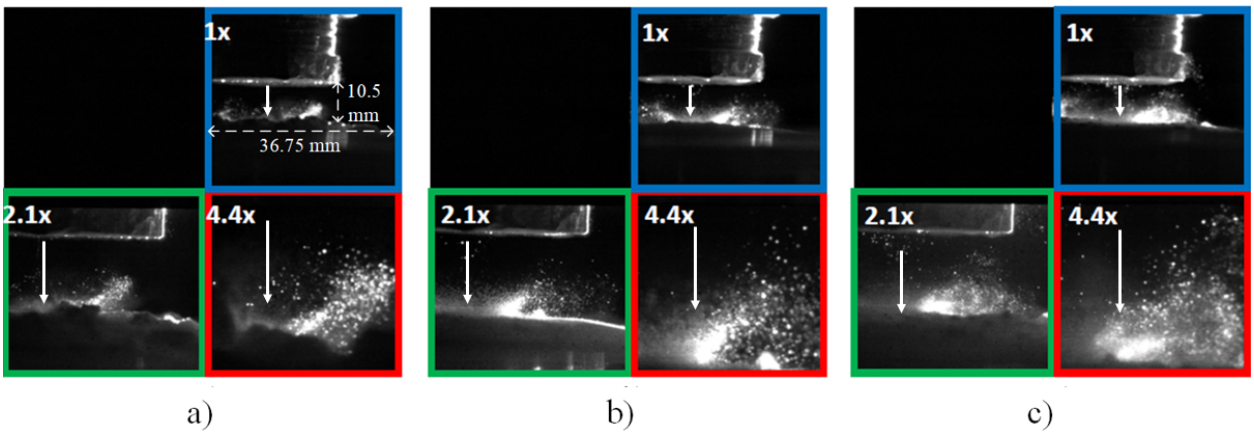

Fig. 11 a) Test 1: small particles. b) Test 2: large particles. c) Test 3: mixed particles. The white arrows indicate the location of the jet plume.

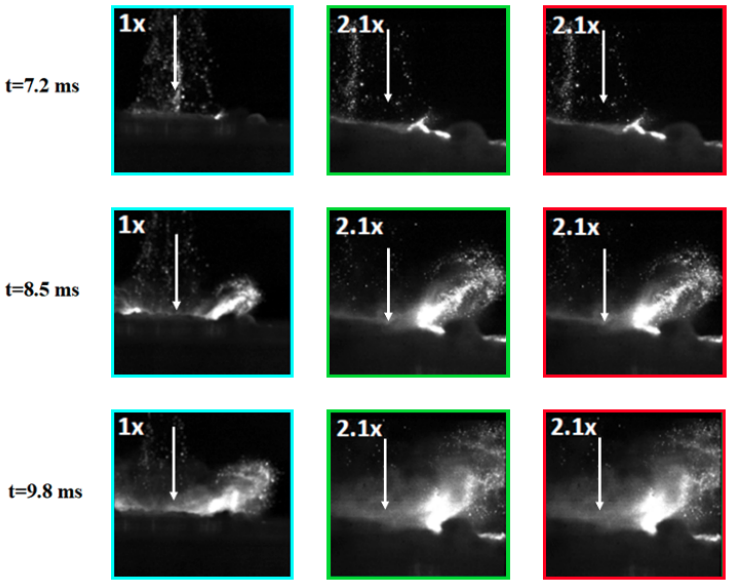

Fig. 12 Multi-resolution views of Test 4 at *h/D*=10: a) full view, b) intermediate view, and c) close-up view using small particles. White arrows indicate location of the jet plume.

The selected images in Fig. 12 demonstrate similar features to those of previous PSI studies where a strong flow shock initiates the formation of the ejecta cloud, shown by the bright angled region in all three images. However, as time increases, a more dispersed ejecta cloud is formed, which causes more haze within the last frame.

The final variation that was studied was the effect of *h/D*. Figure 13 illustrates the mixed particle size for an *h/D* of 3, 10, and 18, which correspond to Tests 3, 6, and 9, respectively. These frames were collected at approximately the same point in time after impingement.

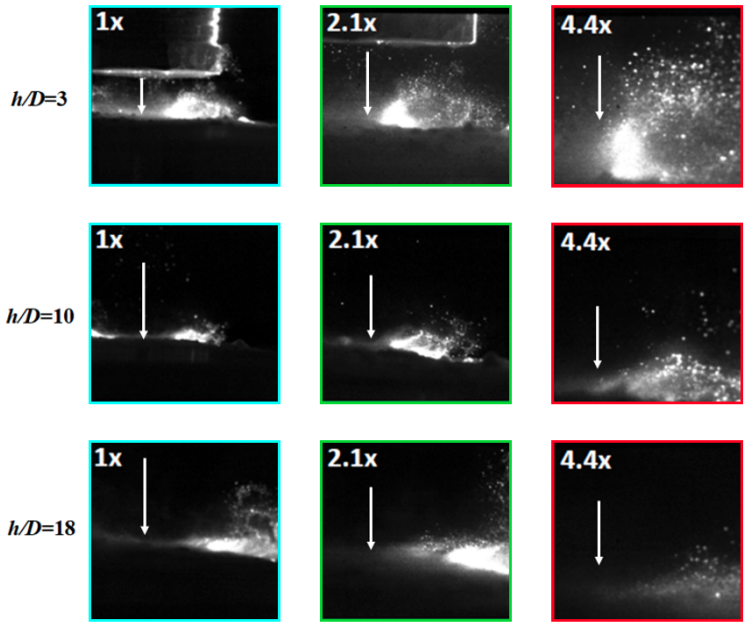

Fig. 13 From top to bottom, comparison of Tests 3, 6, and 9 using a mix of particle sizes at different *h/D* indicated: a) full view b) intermediate view c) close-up view. White arrows indicate the location of the jet plume.

There are several observed effects that increased *h/D* appears to have. Firstly, increasing the *h/D* seems to decrease the ejecta angle. Additionally, the dust cloud, after the initial impact, seems to form more quickly at a higher *h/D*. At a higher *h/D*, the plume hitting the surface of the bed may be larger in diameter, which may cause the particles to spread in a more uniform fashion.

2. PIV Analysis

Ejecta velocities were analyzed using the time-resolved PIV algorithm (LaVision® DaVis 10.2) [38]. The cross-correlation window size, which determines vector density, was adjusted based on the camera field of view (FOV). For close-up, intermediate, and full views, the interrogation windows were set to 16x16, 24x24, and 32x32 pixels, respectively. The maximum expected displacement was set to 8 pixels, based on preliminary analysis of ejecta motion per frame. To reduce noise in static illuminated areas, background subtraction was performed using the first image of each set. A geometric mask was applied to focus measurements on regions of interest (ROI) where ejecta plumes formed adjacent to the main jet center-line. The analysis captured the initial jet plume impingement and its subsequent ejection of particles. The time-resolved velocity evolution of the ejecta plume for Test 5, which used large particles and an *h/D* of 10 is shown in Fig. 14.

As indicated by the vector fields, particles moved away from the plume and increased in velocity over time, consistent with expected behavior. During this ejection phase, localized pockets of higher velocity formed within the plume, with maximum velocities ranging between 12–16 m/s. The white particles featured on the left of the ROI in Fig. 14 are silica particles which were likely aspirated into the nozzle after shutdown on the previous test.

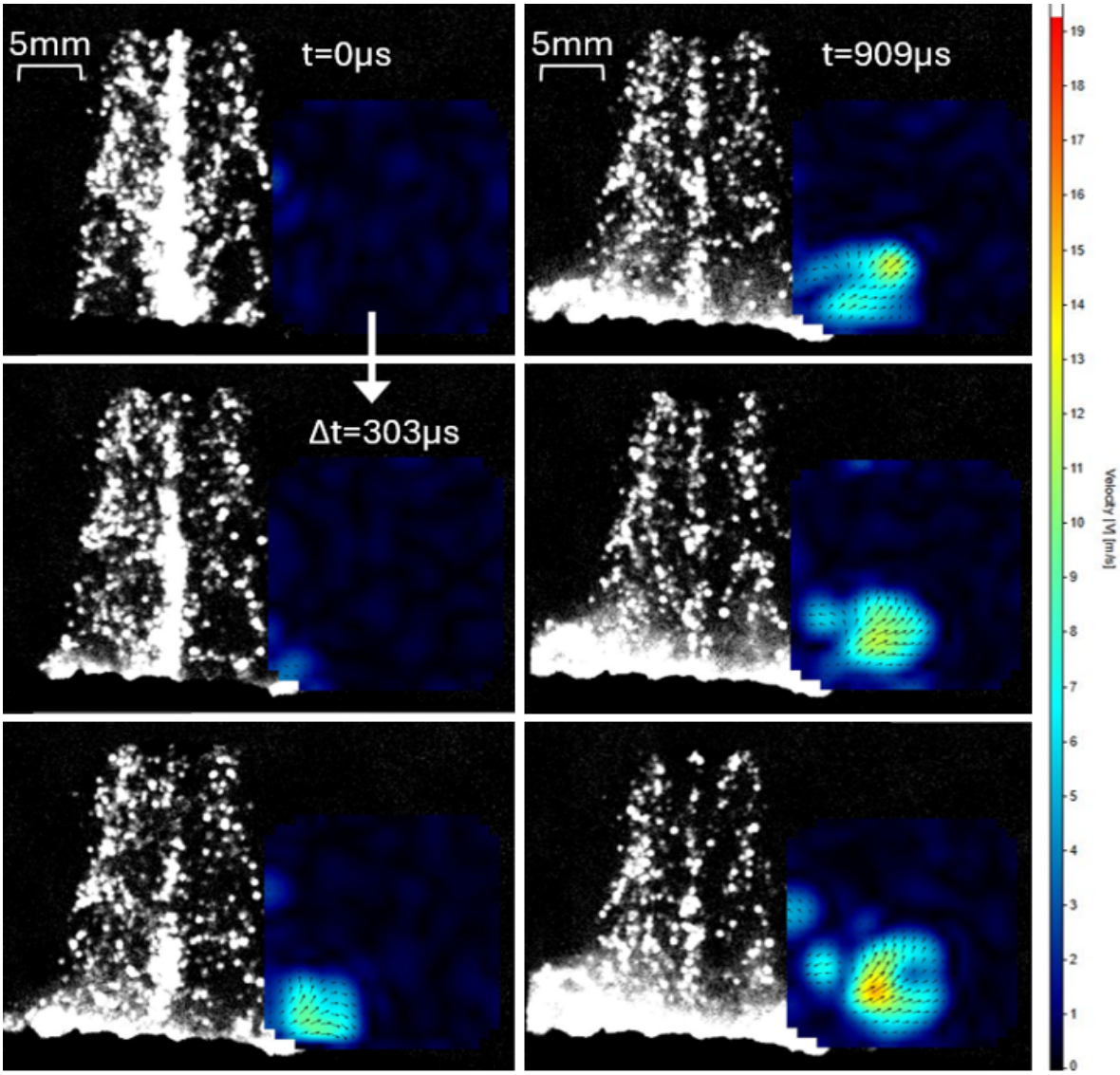

Fig. 14 Time resolved plume evolution for the intermediate view for Test 5 at *h/D*=10. The vertical image interval is 303 µs and the horizontal image interval is 909 µs. The images are composites of the ROI, where PIV analysis was performed and the results were displayed on a color scale, overlaid onto the corresponding source image. The velocity field corresponds to the region it is overlaid on.

The average velocity profiles for each *h/D* ratio are depicted in Fig.15. It is worth noting that the average profiles do not appear to follow the expected trend, and this was evident across all tests. It is expected that ejecta velocity would decrease as *h/D* increases, as the jet plume would expand and lose momentum, imparting less energy over a larger area. There are a couple of possible explanations for this observation. One possibility is that the converging nozzle is a small hole in a much larger flat brass face, which could be interacting with the flow at small *h/D*, locally increasing the pressure and suppressing the velocity. Another explanation is that this may be a result of averaging velocity profiles within the ROI. The averaging may mask variations within the plume, making the profiles less representative of the plume's true dynamics.

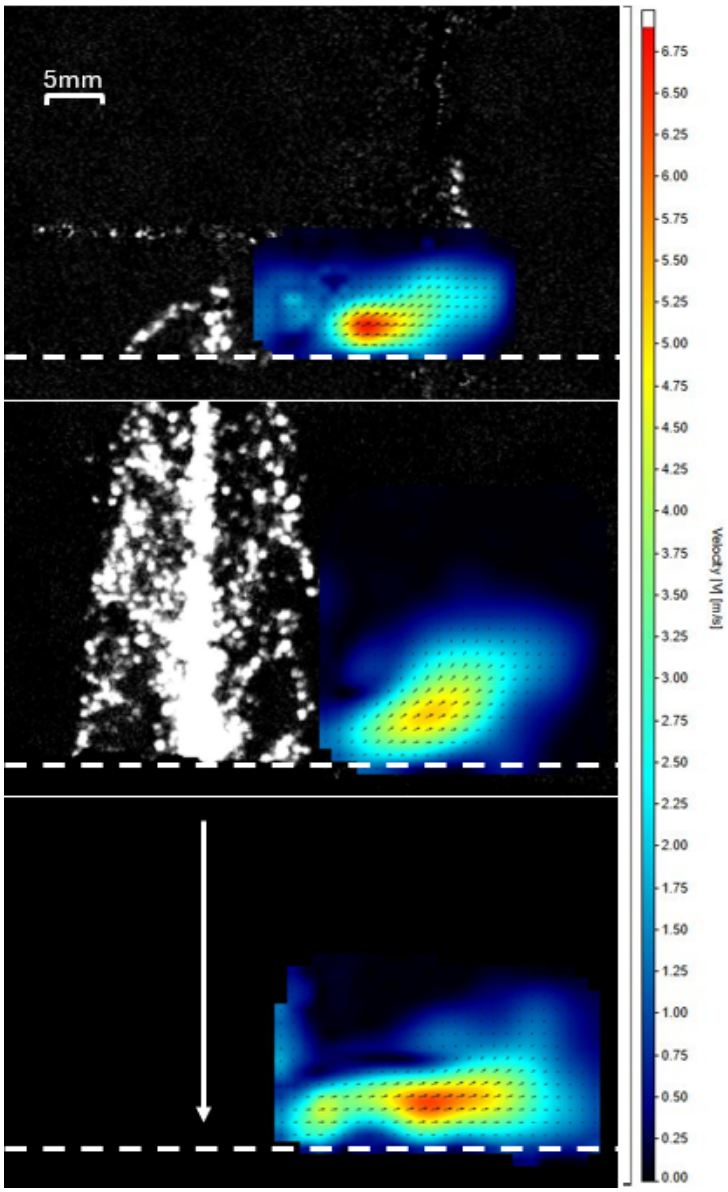

Fig. 15 Averaged velocity profiles based on the far view. From top to bottom: *h/D*=3, 10, 18. The dashed white lines indicate the experimental ground level, and the white arrow indicates the location of the jet plume for the *h/D*=18 test.

Of particular interest were the results of the average vorticity vector fields across all test environments. The averaged field consistently revealed a shear layer separating two regions of high vorticity. The presence of the shear layer corresponds to some of the simulation results found in Ref. [14], where the computed gas pressure profiles suggest a shear layer would be present in this same location. The averaged vorticity field from Test 5, at an *h/D* of 10, is depicted and annotated in Fig. 16. Furthermore, the shear layer was characterized by what appears to be oscillatory behavior. Within the shear layer are multiple cells of low to no vorticity separated by areas of higher vorticity that connect zones 1 and 2. The average vorticity fields for the far view in all test cases are shown in Fig. 17. The angle of the shear layer changes with particle size, suggesting that this phenomenon is highly coupled to the mass of the particles in the ejecta cloud.

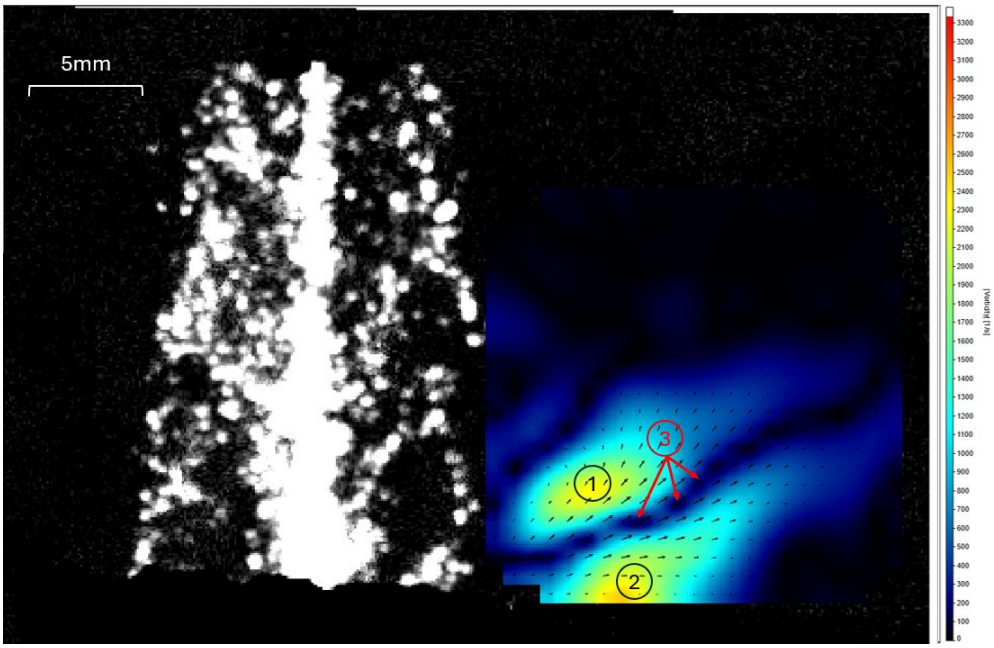

Fig. 16 Averaged vorticity field at the far for Test 5, *h/D*=10. Vortex regions 1 and 2 are separated by the oscillatory shear layer (3), with the cells indicated by the red arrows.

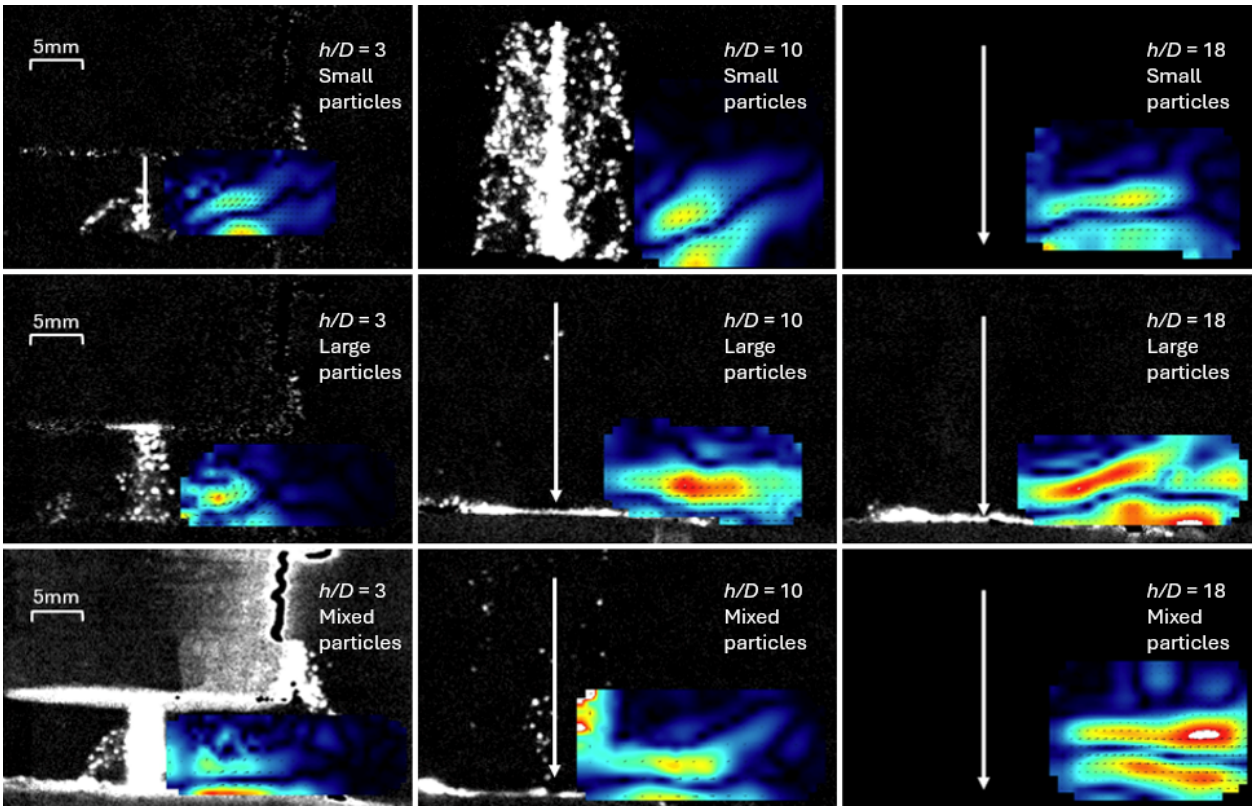

Fig. 17 Averaged vorticity fields at the far view for all test cases. From top to bottom: 8-12.5 µm particles, 65-75 µm particles, mixed particles. From left to right: *h/D*=3, 10, 18. White arrows indicate the location of the jet plume.

B. X-ray Absorption Results

Preliminary tests were conducted at three *h/D* ratios to visualize global ejecta density using X-ray imaging and compare these results with the Mie scattering data. The nozzle produced a Mach 3 jet at its exit, but shock trains and shear layers significantly reduced the jet core velocity as it interacted with the dust clouds under various *h/D* conditions. Figure 18 shows six selected frames from one camera for each of the *h/D* test conditions to demonstrate how the ejecta plume changes with time. These frames were spaced by 10 ms each, i.e. every tenth frame captured by the camera, and begin with the moment the jet makes contact with the surface, illustrated in false blue color to increase contrast. The speed of PSI development varied with *h/D*. At *h/D* = 3, the event concluded by 50 ms, while for *h/D* = 10 and *h/D* = 18, significant particulate activity persisted, indicating longer event durations. The test at *h/D* = 10 displayed a more abrupt plume development than the other cases, potentially influenced by differences in sample surface geometry. Further experiments are required to confirm this observation.

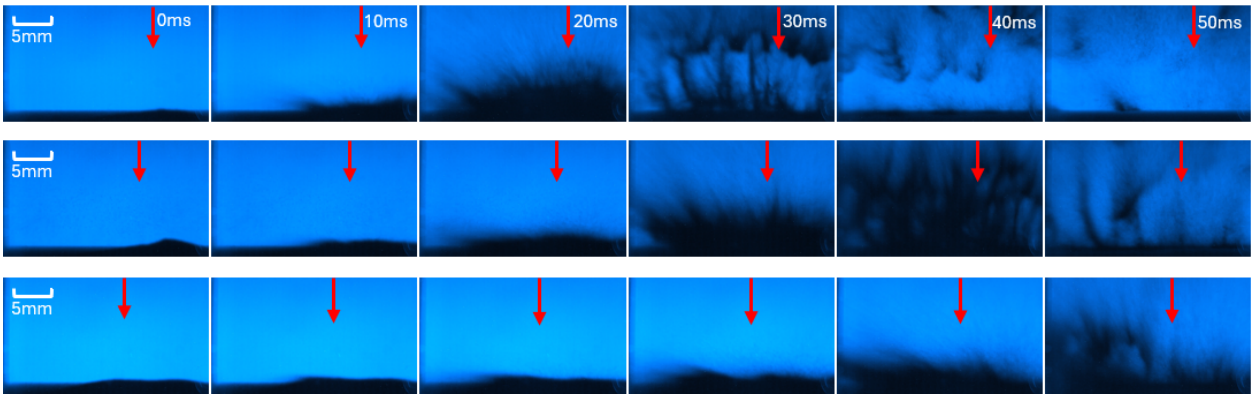

Fig. 18 Time resolved progression of ejecta plume following the impingement of a cold nitrogen jet. From top to bottom: *h/D*=3, 10, 18. Red arrow indicates position of nozzle over the sample.

Figure 19 provides a side-by-side comparison of ejecta plumes captured using laser-scattering and X-ray imaging at *h/D* = 3, approximately 40 ms after jet contact with the surface. The laser-scattered image appears opaque due to high particle density in the view which obscures plume core features. In contrast, the X-ray image clearly resolves flow features within the ejecta plume core, providing direct evidence of the dust cloud core formation—features that have not been previously identified in experiments. It should also be noted that the visible scattering is a planar measurement, while the X-ray absorption is line-of-sight. This is likely a significant reason as to why the images look so different, as the structures revealed by the X-rays are three-dimensional, but are being projected onto a 2D image. It is also possible that the difference in particle size and density between the experiments affected the appearance of the images. The tungsten particles are larger and nearly 8 times denser than the silica glass alternative. This puts the mass of the tungsten particles at 25x that of the large silica particles and over 8700x that of the small silica particles. Thus, it is expected that with these differences, there would be significant discrepancies in the particle behavior across the experiments. While these results are preliminary, they demonstrate the potential of X-ray imaging for studying PSI phenomena. Further improvements are necessary to optimize the method and will be explored in future studies. These include:

- Enhancing the scintillator and light collection system, possibly with an image intensifier for increased signal-to-noise ratio (SNR).
- Improving temporal resolution for better capture of transient phenomena.
- Optimizing the X-ray source alignment and positioning for better image quality
- Integrating a high-speed supersonic jet.
- Selecting dust particles that better match regolith properties for more accurate plume simulation.
- Optimizing the tomographic setup, allowing the use of CT to better discern the differences between the planar and line of sight imaging methods for the two experiments.

These refinements are essential for further characterizing flow behavior in the ejecta plume core. This initial effort highlights X-ray imaging as a viable technique for accessing otherwise obscured regions of PSI.

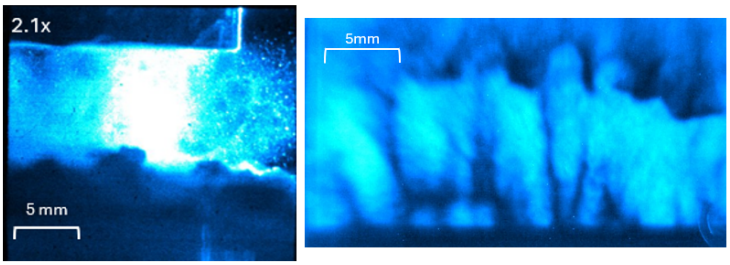

Fig. 19 Ejecta plumes imaged at *h/D*=3 for 532 nm laser illumination at intermediate view (left) and X-ray (right) at ~40 ms after jet impingement.

V. Summary and Conclusions

This preliminary investigation provides some valuable insights into the current understanding of PSI, and future steps to be taken in order to further assist in modeling. The conclusions are as follows:

- This study introduced multi-view scattering imaging at 1x, 2x, and 4x zoom levels, enabling simultaneous observation of PSI interactions across multiple spatial scales. With a temporal resolution of 76 kHz and the potential to reach >100 kHz, this method provides a detailed assessment of fluid-particle interactions across varying spatio-temporal scales.
- Preliminary results revealed flow structures and phenomena consistent with predictions from prior simulation work. Prior simulation work suggests that a shear layer is formed upon impingement of the jet on the surface, and Mie scattering testing revealed a corresponding shear layer, demonstrating that these tools show reasonable results overall.
- Further optimization of the imaging system is needed to more accurately characterize velocity profiles of the ejecta plume with changes in *h/D*.
- Scattering-based measurements faced limitations during the later stages of PSI due to the high density of dust clouds, which rendered visible light ineffective for imaging. To overcome this challenge, X-ray imaging was developed as an alternative diagnostic approach.
- Preliminary X-ray imaging results demonstrated the ability to penetrate opaque dust clouds. This method proved effective in capturing and characterizing complex flow structures within the core of the ejecta plume, which were otherwise obscured by excessive scattering in visible-light experiments.

VI. Acknowledgments

This material is based upon work supported by the National Aeronautics and Space Administration under Grant No.80NSSC23PB580 by the Small Business Innovation Research (SBIR) grant awarded to Spectral Energies, LLC. N. S. Rodrigues and P. M. Danehy acknowledge the support of the NASA Space Technology Mission Directorate GCD program

References

[1] Subramanian, S., Wilson, A., White, C., Kontis, K., Evans, D., and Van den Eynde, J., "Tracking plume-regolith interactions in near-vacuum conditions," *Physics of Fluids*, Vol. 36, No. 1, 2024, p. 013301. https://doi.org/10.1063/5.0180669.

[2] Rubio, J. S., Gorman, M., Diaz-Lopez, M. X., and Ni, R., "Plume-surface interaction physics focused ground test 1: Setup and preliminary results," *AIAA SCITECH 2022 Forum*, 2022, p. 1809. https://doi.org/10.2514/6.2022-1809.

[3] Rahimi, A., Ejtehadi, O., Lee, K., and Myong, R., "Near-field plume-surface interaction and regolith erosion and dispersal during the lunar landing," *Acta Astronautica*, Vol. 175, 2020, pp. 308–326. https://doi.org/10.1016/j.actaastro.2020.05.042.

[4] Jaffe, L. D., "Blowing of lunar soil by Apollo 12: Surveyor 3 evidence," *Science*, Vol. 171, No. 3973, 1971, pp. 798–799. https://doi.org/10.1126/science.171.3973.798.

[5] Metzger, P., Li, X., Immer, C., and Lane, J., "ISRU implications for lunar and martian plume effects," *47th AIAA Aerospace Sciences Meeting including The New Horizons Forum and Aerospace Exposition*, 2009, p. 1204. https://doi.org/10.2514/6.2009-1204.

[6] Aronowitz, L., Koch, F., Scanlon, J. H., and Sidran, M., "Contamination of lunar surface samples by the lunar module exhaust," *Journal of Geophysical Research*, Vol. 73, No. 10, 1968, pp. 3231–3238. https://doi.org/10.1029/JB073i010p03231.

[7] Craig, A., Anzalone, E., Hannan, M., Belanger, B., Burke, L., Condon, G., Joyce, R., Mahajan, B., Means, L., and Pei, J., "Human landing system storable propellant architecture: Mission design, guidance, navigation, and control," *2020 AAS/AIAA Astrodynamics Specialist Conference (Video Presentation)*, 2020. URL https://ntrs.nasa.gov/citations/20205004517.

[8] Korzun, A. M., Eberhart, C. J., West, J., Liever, P., Weaver, A., Mantovani, J., Langton, A., Kemmerer, B., and Atkins, A., "Design of a Subscale, Inert Gas Test for Plume-Surface Interactions in a Reduced Pressure Environment," *AIAA SCITECH 2022 Forum*, 2022. https://doi.org/10.2514/6.2022-1808.

[9] Mehta, M., Sengupta, A., Renno, N. O., Norman, J. W. V., Huseman, P. G., Gulick, D. S., and Pokora, M., "Thruster Plume Surface Interactions: Applications for Spacecraft Landings on Planetary Bodies," *AIAA Journal*, Vol. 51, No. 12, 2013, pp. 2800–2818. https://doi.org/10.2514/1.J052408.

[10] Gorman, M. T., Rubio, J. S., Diaz-Lopez, M. X., Chambers, W. A., Korzun, A. M., Rabinovitch, J., and Ni, R., "Scaling laws of plume-induced granular cratering," *PNAS nexus*, Vol. 2, No. 9, 2023, p. pgad300. https://doi.org/10.1093/pnasnexus/pgad300.

[11] Rahimi, A., Ejtehadi, O., Lee, K., and Myong, R., "Near-field plume-surface interaction and regolith erosion and dispersal during the lunar landing," *Acta Astronautica*, Vol. 175, 2020, pp. 308–326. https://doi.org/10.1016/j.actaastro.2020.05.042.

[12] Roberts, L., "The action of a hypersonic jet on a dusty surface," *Proceedings of 31st Annual Meeting of the Institute of Aerospace Science, New York, NY*, 1963, pp. 63–50.

[13] Roberts, L., "The interface of a rocket exhaust with the lunar surface," *The Fluid Dynamic Aspects of Space Flight*, 1966, pp. 269–290.

[14] Morris, A. B., Goldstein, D. B., Varghese, P. L., and Trafton, L. M., "Lunar dust transport resulting from single-and four-engine plume impingement," *AIAA Journal*, Vol. 54, No. 4, 2016, pp. 1339–1349. https://doi.org/10.2514/1.J054532.

[15] Chinnappan, A. K., Kumar, R., and Arghode, V. K., "Modeling of dusty gas flows due to plume impingement on a lunar surface," *Physics of Fluids*, Vol. 33, No. 5, 2021. https://doi.org/10.1063/5.0047925.

[16] Cao, Z., White, C., Agir, M., and Kontis, K., "Lunar plume-surface interactions using rarefiedMultiphaseFoam," *Frontiers in Mechanical Engineering*, Vol. 9, 2023, p. 1116330. https://doi.org/10.3389/fmech.2023.1116330.

[17] Land, N. S., and Clark, L. V., *Experimental investigation of jet impingement on surfaces of fine particles in a vacuum environment*, National Aeronautics and Space Administration, 1965.

[18] Metzger, P. T., Latta III, R. C., Schuler, J. M., and Immer, C. D., "Craters formed in granular beds by impinging jets of gas," *AIP Conference Proceedings*, Vol. 1145, American Institute of Physics, 2009, pp. 767–770. https://doi.org/10.1063/1.3180041.

[19] Diaz-Lopez, M. X., Gorman, M., Rubio, J. S., and Ni, R., "Plume-surface interaction physics focused ground test 1: Diagnostics and preliminary results," *AIAA Scitech 2022 Forum*, 2022, p. 1810. https://doi.org/10.2514/6.2022-1810.

[20] Rodrigues, N., Tyrrell, O., Danehy, P., Eberhart, C., McDougal, K., Liu, T., Reynolds, T., Rubio, J., Jiang, N., Hsu, P., et al., "Flow Visualization for Plume-Surface Interaction Testing Within Large-Scale Vacuum Environments at Conditions Relevant to Lunar and Martian Landers," *December 2023 Joint Army-Navy-NASA-Air Force (JANNAF) meeting*, 2023. URL https://ntrs.nasa.gov/citations/20230014819.

[21] Rodrigues, N. S., Tyrrell, O. K., Eberhart, C., McDougal, K. J., Korzun, A., and Danehy, P. M., "Flow visualization for plume surface interaction at martian-relevant lander environments," *AIAA AVIATION FORUM AND ASCEND 2024*, 2024, p. 4914. https://doi.org/10.2514/6.2024-4914.

[22] Rodrigues, N., Tyrrell, O., and Danehy, P., "Fluorescence imaging of plume-surface interaction in large-scale reduced pressure environments," *Physics of Fluids*, Vol. 36, No. 10, 2024. https://doi.org/10.1063/5.0223210.

[23] Tyrrell, O. K., Rodrigues, N. S., Korzun, A. M., and Danehy, P. M., "Flow visualization of intrusive and non-intrusive configurations for lunar-and Martian-relevant plume-surface interaction," *AIAA SCITECH 2024 Forum*, 2024, p. 2499. https://doi.org/10.2514/6.2024-2499.

[24] Eberhart, C. J., West, J., and Korzun, A. M., "Overview of plume-surface interaction data from subscale inert gas testing at NASA MSFC test stand 300 vacuum facilities," *AIAA Scitech 2022 Forum*, 2022, p. 1811. https://doi.org/10.2514/6.2022-1811.

[25] Upadhyay, A., Lengden, M., Enemali, G., Stewart, G., Johnstone, W., Wilson, D., Humphries, G., Benoy, T., Black, J., Chighine, A., et al., "Tomographic imaging of carbon dioxide in the exhaust plume of large commercial aero-engines," *Applied optics*, Vol. 61, No. 28, 2022, pp. 8540–8552. https://doi.org/10.1364/AO.467828.

[26] Meyer, T. R., Halls, B. R., Jiang, N., Slipchenko, M. N., Roy, S., and Gord, J. R., "High-speed, three-dimensional tomographic laser-induced incandescence imaging of soot volume fraction in turbulent flames," *Optics express*, Vol. 24, No. 26, 2016, pp. 29547–29555. https://doi.org/10.1364/OE.24.029547.

[27] Weiss, L., Wensing, M., Hwang, J., Pickett, L. M., and Skeen, S. A., "Development of limited-view tomography for measurement of Spray G plume direction and liquid volume fraction," *Experiments in Fluids*, Vol. 61, 2020, pp. 1–17. https://doi.org/10.1007/s00348-020-2885-0.

[28] Kalender, W. A., "X-ray computed tomography," *Physics in medicine & Biology*, Vol. 51, No. 13, 2006, p. R29. https://doi.org/10.1088/0031-9155/51/13/R03.

[29] Cai, W., Powell, C. F., Yue, Y., Narayanan, S., Wang, J., Tate, M. W., Renzi, M. J., Ercan, A., Fontes, E., and Gruner, S. M., "Quantitative analysis of highly transient fuel sprays by time-resolved x-radiography," *Applied Physics Letters*, Vol. 83, No. 8, 2003, pp. 1671–1673. https://doi.org/10.1063/1.1604161.

[30] Liu, X., Im, K.-S., Wang, Y., Wang, J., Tate, M. W., Ercan, A., Schuette, D. R., and Gruner, S. M., "Four dimensional visualization of highly transient fuel sprays by microsecond quantitative x-ray tomography," *Applied Physics Letters*, Vol. 94, No. 8, 2009. https://doi.org/10.1063/1.3048563.

[31] Bieberle, M., Fischer, F., Schleicher, E., Koch, D., Menz, H.-J., Mayer, H.-G., and Hampel, U., "Experimental two-phase flow measurement using ultra fast limited-angle-type electron beam X-ray computed tomography," *Experiments in fluids*, Vol. 47, 2009, pp. 369–378. https://doi.org/10.1007/s00348-009-0617-6.

[32] Duke, D. J., Swantek, A. B., Sovis, N. M., Tilocco, F. Z., Powell, C. F., Kastengren, A. L., Gürsoy, D., and Biçer, T., "Time-resolved x-ray tomography of gasoline direct injection sprays," *SAE International Journal of Engines*, Vol. 9, No. 1, 2016, pp. 143–153. https://doi.org/10.4271/2015-01-1873.

[33] Collard, D. N., McClain, M. S., Rahman, N. A., Dorcy, N. H., Meyer, T. R., and Son, S. F., "Dynamic X-Ray Imaging of Additively Manufactured Reactive Components in Solid Propellants," *Journal of Propulsion and Power*, Vol. 37, No. 3, 2021, pp. 362–368. https://doi.org/10.2514/1.B38128.

[34] Karpetis, A. N., Ellis, D. W., and Bayeh, A. C., "Miniature Supersonic Burner for the Study of Combustion at Extreme Conditions. I: Internal Flow," *Journal of Energy Engineering*, Vol. 144, No. 5, 2018. https://doi.org/10.1061/(asce)ey.1943-7897.0000573.

[35] Carrier III, W. D., "Lunar soil grain size distribution," *The moon*, Vol. 6, No. 3, 1973, pp. 250–263. https://doi.org/10.1007/BF00562206.

[36] Fiksel, G., Marshall, F., Mileham, C., and Stoeckl, C., "Note: Spatial resolution of Fuji BAS-TR and BAS-SR imaging plates," *Review of Scientific Instruments*, Vol. 83, No. 8, 2012. https://doi.org/10.1063/1.4739771.

[37] Halls, B., Gord, J., Schultz, L., Slowman, W., Lightfoot, M., Roy, S., and Meyer, T., "Quantitative 10–50 kHz X-ray radiography of liquid spray distributions using a rotating-anode tube source," *International Journal of Multiphase Flow*, Vol. 109, 2018, pp. 123–130. https://doi.org/10.1016/j.ijmultiphaseflow.2018.07.014.

[38] LaVision GmbH, *DaVis 10.2 Software*, Göttingen, Germany, November 2022. URL https://www.lavision.de/en/downloads/manuals/systems.php, product manual for particle image velocimetry (PIV) software.